Velocity Estimation of Spots in Three-Dimensional Confocal Image Sequences of Living Cells

C.B.J. Bergsma,[1*] **G.J. Streekstra,**[2] **A.W.M. Smeulders,**[1] **and E.M.M. Manders**[3]

[1]Intelligent Sensory Information Systems, Faculty of Science, University of Amsterdam, Amsterdam, The Netherlands
[2]Department of Medical Physics, Academic Medical Center, University of Amsterdam, Amsterdam, The Netherlands
[3]Swammerdam Institute for Life Sciences, Faculty of Science, University of Amsterdam, Amsterdam, The Netherlands

Background: The analysis of three-dimensional (3D) motion is becoming increasingly important in life cell imaging. A simple description of sometimes complex patterns of movement in living cells gives insight in the underlying mechanisms governing these movements.
Methods: We evaluate a velocity estimation method based on intensity derivatives in spatial and temporal domain from 3D confocal images of living cells. Cells of the sample contain intense spots throughout the cell nucleus. In simulations, we model these spots as Gaussian intensity profiles which are constant in intensity and shape. To quantify the quality of the estimated velocity, we introduce a reliability measure.
Results: For constant linear velocity, the velocity estimation is unbiased. For accelerated motion paths or when a neighboring spot disturbs the intensity profile, the method results are biased. The influence of the point-spread function on the velocity estimation can be compensated for by introducing anisotropic derivative kernels. The insight gained in the simulations is confirmed by the results of the method applied on an image sequence of a living cell with fluorescently labeled chromatin.
Conclusions: With the velocity estimation method, a tool for estimating 3D velocity fields is described which is successfully applied to a living cell sequence. With the estimated velocity fields, motion patterns can be observed, which are a useful starting point for the analysis of dynamic processes in living cells. Cytometry 43:261–272, 2001. © 2001 Wiley-Liss, Inc.

Key terms: 3D velocity estimation; spot motion; optical flow; confocal microscope; point-spread function; living cells; image analysis

During the last few years, new labeling techniques (e.g., GFP techniques and in vitro labeling of DNA with fluorescent nucleotide) and detection techniques (e.g., confocal microscopy and two-photon excitation) have become available that allow us to observe cellular structures in three dimensions (3D) in living cells. The data generated by 4D imaging (3D + time) contains the information concerning the complex movements of these structures. Therefore, determination of 3D motion patterns of spots is of major importance. Velocity estimates of individual spots can provide valuable information in analysis of motion patterns.

Velocity estimation methods can be roughly divided into two groups: feature and model-based object tracking methods (1,2) and image derivative-based methods like optical flow (3–8). Spot tracking methods rely heavily on the accuracy of the segmentation of spots or other uniquely detectable characteristic objects. In general, segmentation methods are sensitive to the high noise levels, which are common in image sequences of living cells. No segmentation is needed with optical flow methods. Consequently, motion patterns can be obtained avoiding the disadvantages related to segmentation.

Practical imaging with a confocal system results in blurred images of spots (9). The blurring is caused by the point-spread function of the system. When the objects are small compared to the point-spread function, the blurring can cause a biased velocity estimation. Usually, deconvolution is used to reduce the influence of blurring by the point-spread function. However, deconvolution is noise sensitive (10) and complete reconstruction of the original objects is never accomplished. Therefore, we have developed a procedure that allows the compensation for blurring by the point-spread function. This procedure is incorporated in the velocity estimation method without any loss of functionality and computational efficiency of the velocity estimation method.

In this study, we evaluate the applicability of optical flow on 3D image sequences containing moving spots. We show that this method is theoretically unbiased for con-

*Correspondence to: C.B.J. Bergsma, Intelligent Sensory Information Systems, Faculty of Science, University of Amsterdam, Kruislaan 403, 1098 SJ Amsterdam, The Netherlands.
E-mail: kees@wins.uva.nl

stant motion of a single spot along a straight trajectory. We also investigate the velocity estimation for curved trajectories of single spots and linear trajectories with overlapping spots and introduce a reliability measure. A correction procedure was designed to compensate for the influence of the point-spread function. The applicability of the methods presented here is demonstrated in two different image sequences recorded by confocal microscopy: fluorescent beads and fluorescently labeled chromatin in living cells (11).

MATERIALS AND METHODS
Optical Flow

The formulation of optical flow is based on the assumption that the total time derivative of the image is zero at all positions through the image sequence. This leads to the optical flow constraint as introduced by Horn and Schunk (6):

$$\nabla I(\mathbf{x}, t) \cdot \mathbf{v}(\mathbf{x}, t) + I_t(\mathbf{x}, t) = \mathbf{0}, \qquad (1)$$

with $I(\mathbf{x}, t)$ the image intensity function,

$$\nabla I(x, t) = (\partial I(x, t)/\partial x, \partial I(x, t)/\partial y, \partial I(x, t)/\partial z)$$

the gradient vector of the image intensity, $I_t(\mathbf{x}, t)$ the time derivative of the intensity, and position is the 3D $\mathbf{x} = (x, y, z)$. Vector $\mathbf{v}(x, t)$ is the optical flow at position and time of computation of derivatives. The optical flow vector corresponds to the 3D velocity vector at a certain position in space.

In case the space would be 1D, a single optical flow constraint is theoretically sufficient to compute a single velocity vector. The single linear equation (1) does not yield sufficient information to resolve the velocity from a sequence of 3D images regarding the 3D nature of flow vector $\mathbf{v}(x, t)$; the system is underdetermined. Several solutions for extra constraints are available: multiple measurements in a single point (5,12), an extra global constraint (6), and a local motion constraint (7,8).

Multiple measurements in a single point require multiple independent filters applied to the image. For example, application of different orders of derivatives or different orientations of derivative filters is used (12). The computational load increases with the amount of independent filters and higher-order derivatives are more sensitive to noise. Consequently, for the noisy images of living cells, first-order derivatives are more appropriate.

The global motion constraint assumes small variation in the motion over the total image domain. In a sequence with multiple spots, spots have different individual velocities. Accordingly, estimations using a global motion constraint will be biased in living cell image sequences. Therefore, the velocity is calculated using a local motion constraint (4,7,8). The assumption in using local constraints is that neighboring voxels within a local region Ω will have the same velocity and should give the same optical flow vector. In computing the flow vector, a number of optical flow constraint equations within a small region around the position of flow estimation are combined. To emphasize information close to the point of estimation, a weighting function is used which decays with distance from the central position.

We compute the optical flow following (3,4,7,8). To find the flow vector, we compute a linear least squares estimation of $\mathbf{v}(x, t)$ with a Gaussian weight function $W(x)$. The weight function is incorporated in a squared error function by a convolution of the squared optical flow constraint with $W(x)$

$$E(\mathbf{v}(\mathbf{x}, t)) = W(\mathbf{x}) * [\nabla I(\mathbf{x}, t) \cdot \mathbf{v}(\mathbf{x}, t) + I_t(\mathbf{x}, t)]^2, \qquad (2)$$

with

$$W(x) = \frac{1}{\sqrt{2\pi\sigma_w^2}} e^{-(|x|^2/2\sigma_w^2)}. \qquad (3)$$

Equation (2) gives the error function in every position in the image sequence. Minimizing the error function (2) for

$$\nabla_{\mathbf{v}} E(\mathbf{v}) = W(\mathbf{x}) * [\nabla I(\mathbf{x}, t) \nabla I(\mathbf{x}, t)^T \cdot \mathbf{v}(\mathbf{x}, t)$$
$$+ \nabla I(\mathbf{x}, t) I_t(\mathbf{x}, t)] = \mathbf{0}, \qquad (4)$$

and using the assumption of $\mathbf{v}(x, t)$ constant in $W(x)$ results in an expression for the flow vector $\mathbf{v}(x, t)$:

$$\mathbf{v}(\mathbf{x}, t) = -\mathbf{A}(\mathbf{x}, t)^{-1} \mathbf{b}(\mathbf{x}, t). \qquad (5)$$

In equation (5) matrix $\mathbf{A}(x, t)$ and vector $\mathbf{b}(x, t)$ are defined by:

$$\mathbf{A}(\mathbf{x}, t) = W(\mathbf{x}) * [\nabla I(\mathbf{x}, t) \nabla I(\mathbf{x}, t)^T], \qquad (6)$$

$$\mathbf{b}(\mathbf{x}, t) = W(\mathbf{x}) * [\nabla I(\mathbf{x}, t) I_t(\mathbf{x}, t)]. \qquad (7)$$

The derivative images in Equations (6) and (7) are based on spatiotemporal Gaussian derivatives as used in (12,13):

$$I_t(x, t) = \frac{\partial}{\partial_i} (g(x, t; \sigma_s, \sigma_t) * I(x, t))$$
$$= g_i(x, t; \sigma_s, \sigma_t) * I(x, t), \qquad (8)$$

with i the index of differentiation ($i = x, y, z, t$) of arbitrary order. The Gaussian kernel for derivative function (8) is then:

$$g(x, t; \sigma_s, \sigma_t) = \frac{1}{(\sqrt{2\pi\sigma_s^2})^3} e^{-(|x|^2/2\sigma_s^2)} \frac{1}{\sqrt{2\pi\sigma_t^2}} e^{-(t^2/2\sigma_t^2)}, \qquad (9)$$

with σ_s spatial width and σ_t temporal width of the Gaussian derivative function. Gaussian derivative functions are utilized to suppress the influence of noise on the deriva-
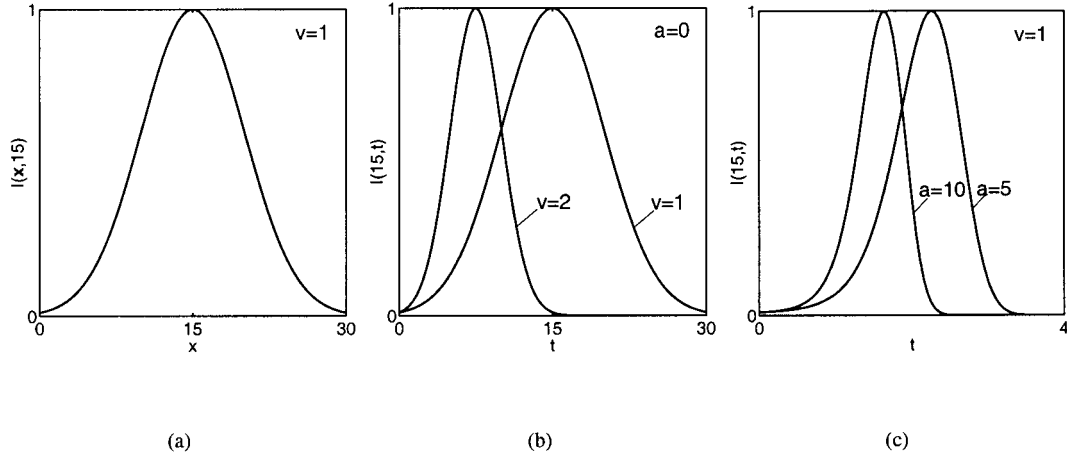
FIG. 1. Intensity profiles in the spatial and the temporal domain for a Gaussian object with σ=5. **a:** A spatial intensity profile (x =15). **b:** Temporal intensity profiles of (a) for two different velocities v={1,2}. **c:** Temporal intensity profiles for two accelerated spots, with acceleration a={5,10}.

tive estimates. Moreover, Gaussian derivatives provide meaningful derivatives in a discrete image (14).

Single-Spot Motion Estimation

Consider an image sequence containing spots moving in a 3D environment. All spot intensity profiles contribute to the image intensity. Here we consider spots to be modeled by a Gaussian intensity profile. For a single moving spot, with width σ, the image sequence intensity function $I(\mathbf{x},t)$ is:

$$I(x,t) = \frac{1}{(\sqrt{2\pi\sigma^2})^3}\, e^{-|x-s(t)|^2/2\sigma^2}, \qquad (10)$$

with the trajectory of the spot described by $\mathbf{s}(t)$.

For a single spot moving along a straight line with constant velocity, the estimation will be unbiased. For unbiased results, error function (2) is equal to zero throughout the image, that is,

$$E(\mathbf{v}) = \mathbf{0}. \qquad (11)$$

Equation (11) is zero if the optical flow constraint (1) is met. In a straightforward derivation, one can prove that with a Gaussian intensity profile and Gaussian derivatives the latter requirement is fulfilled (15).

For accelerated motion, the velocity estimation is expected to be biased. To investigate the mechanism that may introduce the bias due to acceleration, we look at the temporal intensity profile at a constant position in the image (Fig. 1). The position is located on the trajectory of the spot center. When a Gaussian spot is moving along the linear trajectory, the intensity in this constant position changes over time. Plotting the observed intensity as a function of time gives a temporal intensity profile (Fig. 1b). The temporal intensity profile is a symmetric function for a constant velocity along a straight line. The width of

the profile is a relation between the width of the spot and the velocity of the spot.

$$\sigma_{\text{temporal}} = \sigma/|\mathbf{v}|. \qquad (12)$$

If we let the Gaussian spot accelerate, the temporal intensity function becomes asymmetric (Fig. 1c). Because we use symmetric kernels for derivatives and weighting function, we expect the asymmetry to be of influence on the bias of the estimation of the spot velocity.

Reliability Measure

The velocity estimation method assumes a constant intensity profile in a local volume Ω. This is true for single spots. When two spots are close to each other, the intensity profiles overlap. When intensity profiles overlap, the spot intensity profiles are not constant in time anymore. When the intensity of a spot changes over time, bias in the velocity estimation is expected. To detect errors in the velocity field, the smoothness of the local velocity field structure is useful to provide for a reliability measure for the estimated velocity.

The velocity field is called smooth when all vectors in a volume Ω have the same orientation and the same length. This is the case for an unperturbed spot. A smoothness measure of the velocity field can be calculated by principal components analysis (16) of the relative velocity field in a local volume Ω. A velocity $\boldsymbol{v}_r(\mathbf{x},t)$, relative to the average velocity vector $\bar{\boldsymbol{v}}_\Omega$ in volume Ω, is calculated by

$$\mathbf{v}_r(\mathbf{x},t) = \mathbf{v}(\mathbf{x},t) - \bar{\mathbf{v}}_\Omega. \qquad (13)$$

From $\boldsymbol{v}_r(\mathbf{x},t)$, we form a scatter matrix

$$S(\mathbf{x},t) = \overline{\mathbf{v}_r(\mathbf{x},t)\mathbf{v}_r(\mathbf{x},t)^{\mathrm{T}}}, \qquad (14)$$

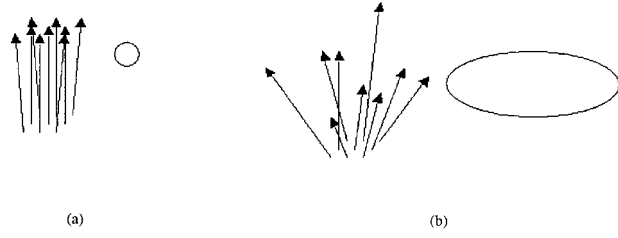(a)   (b)

FIG. 2. Two different examples of a 3D velocity field in a local volume Ω. To the left of each figure, the velocity field is depicted. To the right of each figure, the resulting volume spanned by the eigenvectors $\lambda_1(x,t)$ of the scatter matrix $S(x,t)$ is schematically given. **a:** A small deviation from the average velocity vector causes a small volume spanned by the eigenvectors. **b:** For large deviations of the velocity vectors from the average, a large volume is spanned by the eigenvectors.

FIG. 3. The convolution of an imaged object **(left)** with the anisotrope cigar-shaped point-spread function of the confocal imaging system and an anisotrope oblate ellipsoid kernel of the derivatives leads to an isotrope object image **(right)**. The lateral scale is the scale in x and y direction ($\sigma_1 = \sigma_x = \sigma_y$), the axial scale σ_a is the scale in the z direction. The scale of the isotrope object image is a function of the original object size and the scales of the point-spread function and the kernels σ_g^l and σ_g^a.

where the averaging is over all points in Ω. The eigenvalues $\lambda_i(x,t)$ ($i=1,2,3$) of scatter matrix $S(x,t)$ represent the smoothness of the velocity field in Ω, because the eigenvalues measure the spread of the vectors $v_r(x,t)$ in Ω (Fig. 2). Due to the nature of the relative velocity vector field $v_r(x,t)$, a smooth velocity field gives rise to small eigenvalues (Fig. 2a) because all velocity vectors have the same length and orientation. With such a field, the deviation of the relative velocity from the average velocity in Ω will be zero or at least very small.

Thus, a smooth velocity field will yield small eigenvalues λ_i. Therefore, we define a reliability measure $R(x,t)$, which takes the spread of the velocity field in volume Ω relative to the measured average velocity in volume Ω.

$$R(x,t) = \frac{\bar{v}(x,t)}{\bar{v}(x,t) + \sqrt{\sum_{i=1}^{3} \lambda_i}} \quad (15)$$

with λ_i the eigenvalues of the scatter matrix $S(x,t)$ and $\bar{v}(x,t)$ the average velocity in a local volume Ω with Ω at location and at time point t. The reliability measure is a normalized function, resulting in values between 0 and 1. A value of 1 represents a maximal reliability of the velocity estimation. Smaller values of $R(x,t)$ represent lower reliability.

Anisotropy of the Point-Spread Function

As discussed above, image sequences with isotropic spots and kernels were assumed. However, the actual point-spread function in a confocal microscope is an anisotrope function, which can be approximated by a 3D Gaussian function (17) (in the following denoted by $H(x)$). The size of $H(x)$ in the axial direction (σ_H^a) is approximately three times the size in the lateral direction (σ_H^l) for a 1.3 NA objective. This anisotropy is expected to cause the estimation to be direction dependent if the size of $H(x)$ is in the order of magnitude of the spots to be observed. Consequently, two spots touching in the axial direction experience the same amount of overlap at larger distances than spots touching in the lateral direction. This
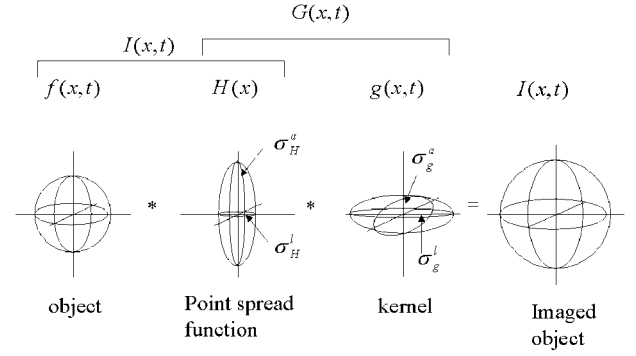
influences the determination of the derivatives involved in the velocity estimation. In this section, we describe how to overcome this position and orientation dependency of the velocity estimate.

A single spot as imaged by a confocal microscope is the result of a convolution of the original object $f(x,t)$ with the point-spread function $H(x)$,

$$I(\mathbf{x},t) = H(\mathbf{x},t)*f(\mathbf{x},t). \quad (16)$$

The Gaussian derivative image of the spot image is a convolution of the spot image $I(x,t)$ with the Gaussian derivative kernel $g_i(x,t)$,

$$I_i(x,t) = \frac{\partial}{\partial i} \left(g(x,t;\sigma_g^l,\sigma_g^a)*H(x,t;\sigma_H^l,\sigma_H^a) \right)*f(x,t). \quad (17)$$

The convolution of two Gaussian functions, $g(x,t;\sigma_g^l,\sigma_g^a)$ and $H(x,t;\sigma_H^l,\sigma_H^a)$ results in a Gaussian function $G(x,t;\sigma_G^l,\sigma_G^a)$ (Fig. 3), with lateral and axial scales:

$$\sigma_G^l = \sqrt{\sigma_g^{l2} + \sigma_H^{l2}}, \quad (18)$$

$$\sigma_G^a = \sqrt{\sigma_g^{a2} + \sigma_H^{a2}}. \quad (19)$$

Thus, the resulting derivative of the spot is an isotrope function if the Gaussian function $G(x,t;\sigma_G^l,\sigma_G^a)$ is an isotrope function. $G(x,t;\sigma_G^l,\sigma_G^a)$ can be made isotrope if σ_g^l and σ_g^a are chosen as follows:

$$\sigma_G^l = \sigma_G^a = \sigma_G \quad (20)$$

$$\sigma_g^l = \sqrt{\sigma_G^2 - \sigma_H^{l2}} \quad (21)$$

$$\sigma_g^a = \sqrt{\sigma_G^2 - \sigma_H^{a2}} \quad (22)$$

Error Measures

To have an indication of the possible bias of the estimated velocity field, error measures are needed. In the simulations, the original motion of the spot is known. Therefore, it is possible to calculate the difference between the original correct velocity v_c and the estimated velocity v_{est}. The definitions of the two error measures employed are:

$$\varepsilon_v = \frac{\left| v_c(x,t) \right| - \left| v_{est}(x,t) \right|}{\left| v_c(x,t) \right|}, \tag{23}$$

$$\varepsilon_\vartheta = \frac{1}{2\pi} \arccos \frac{v_c(x,t) \cdot v_{est}(x,t)}{\left| v_c(x,t) \right| \left| v_{est}(x,t) \right|} \tag{24}$$

In the experiments ε_v is expressed in percentages and ε_θ is expressed in degrees.

Sample Preparation

Cell culture and preparation. Indian Muntjac cells were cultured in glass-bottom Petri dishes coated with poly-d-lysine (MatTek, Ashland, MA). Cells were bead loaded with fluorescein-dUTP (Molecular Probes, Eugene, OR) as described previously (11) and cultured for 5 h to allow incorporation of fluorescein-12-dUTP into nascent DNA. During imaging, the cells were kept at 37°C on a heated stage by using an objective heater (Bioptechs, Butler, PA). 3D images were obtained using a Zeiss LSM510 (Carl Zeiss, Jena, Germany) equipped with a Plan-Neofluar 100x/1.3-oil and Ar-ion laser. To prevent cell death, the laser was tuned at 488 nm and less than 500 nW laser power at the position of the cells (11). Thirty 3D images, each containing 18 optical sections (512 × 512 pixels), were scanned at a sample frequency of 12 images per hour and a voxel size of 60 nm lateral and 300 nm axial. Cells were scanned directly after telophase entering G_1 phase (Manders et al., unpublished data).

Bead preparation. A fluorescent bead with a diameter of 1 μ is imaged with a Zeiss LSM510 equipped with a Plan-Neofluar 100x/1.3-oil and Ar-ion laser tuned at 488 nm. Fifteen 3D images, each containing 64 optical sections (512 × 512 pixels), were scanned with a voxel size of 20 nm lateral and 100 nm axial. Afterwards, a linear motion path is constructed by computing images which are translated relative to the original images. For each individual time frame, a different image is used. In this way, successive frames have uncorrelated noise and imaging imperfections. The bead has a radius R_b in the lateral plane of approximately 25 voxels.

RESULTS

We show examples that demonstrate the applicability of motion estimation on moving spots in 3D. We present a series of simulations that show estimation bias in linear motion, constant and accelerated motion, and curved motion of a single spot. The estimation bias of close spots with overlapping intensity profiles is examined. A final simulation demonstrates the robustness of the motion estimation method in relation to the constant shape of the intensity profile of the spots.

We also demonstrate the application of motion estimation on two image sequences recorded with a confocal microscope. The first image sequence is based on a number of 3D images of a fluorescent bead. The second sequence is a time series of 3D images of a living cell recorded during cell division.

Simulations on Motion

In the simulations, the average error and the standard deviation of the errors ε_v (23) and ε_θ (24) are calculated over a local volume. The local averaging volume is an isotropic volume of the size of the spots. Besides the errors ε_v and ε_θ, the reliability measure R (2.3) is also calculated over the same local averaging volume. In this way, the reliability measure can be compared with the real estimation bias.

The simulations evaluate the estimation bias of the method in three ways: the influence of the type of motion pattern of the spots, the influence of the point-spread function, and the robustness for the shape of the spots. The different motion patterns under evaluation are linear and curved motion. With linear motion, a further classification is made in constant linear motion and accelerated linear motion. In the motion pattern simulations, image sequences are created with the specific motion patterns of a single isotropic Gaussian spot with scale $\sigma=5$.

Experiments reveal that spatial sampling is not critical as long as the spatial scale of the derivative kernels (see equation 9) $\sigma_s \geq 2$ approximately. We choose for σ_s a value of $\sigma_s=0.4\sigma$ and for spatial scale of local volume $W(x)$ (see equation 2) a value of $\sigma_w=\sigma$. Because the time sampling is the most critical parameter in the application of the motion estimation, the temporal kernel size is varied from $\sigma_t=2/3$ to $\sigma_t=2$ in unit time step throughout all simulations.

Linear motion. The estimation bias for the spot moving with constant relative velocity is in the order of $1 \cdot 10^{-3}$ for the temporal filter widths used. The value for the relative velocity $|v|/\sigma$ lies between $|v|/\sigma=0$ and $|v|/\sigma=1$. The deviation of the values of R from the perfect situation ($R = 100\%$) is negligible.

Figure 4 shows the estimation bias for accelerated motion. As expected, bias is a function of the acceleration of the spot and of the scale σ_t of the temporal part of the derivative kernels. The acceleration $a \in [0,0.35]$ is a realistic choice of parameters considering practical motion situations. The motion is chosen in such a way that the velocity at the time point of motion estimation is the same for all the situations $|v|/\sigma = 0.5$. Figure 4 shows a relationship between the temporal size of the kernel and the estimation bias. For small kernels, the bias is small and the bias increases with increasing kernel size. The bias increases with increasing acceleration of the moving spot. The reliability measure decreases with increasing acceleration and increasing kernel size.
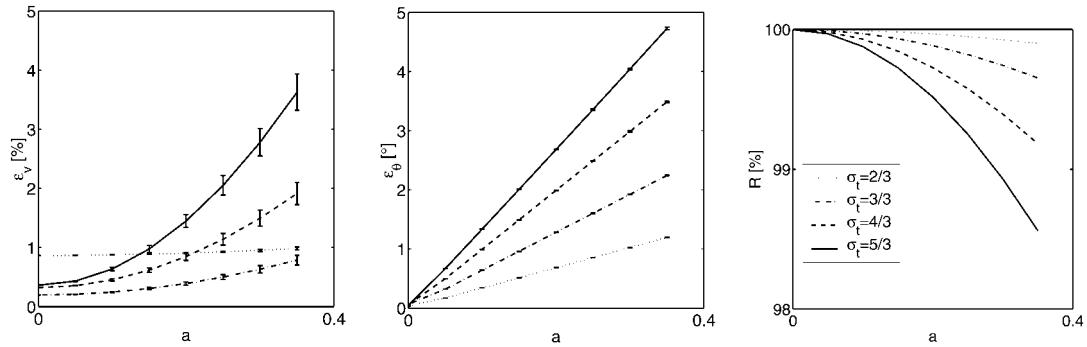
FIG. 4. Accelerated linear motion. For a linear moving Gaussian spot, the velocity estimation errors ε_v and ε_θ and the reliability measure R are given as function of the acceleration of the spot.

Curved motion. Figure 5 shows the estimation bias as a function of the radius of a motion curve (r/σ between $r/\sigma=0$ and $r/\sigma = 20$). The tangential velocity of the spot is kept constant during the simulation ($|v|/\sigma=0.5$). With decreasing radius of the motion curve, the reliability measure decreases significantly compared with the linear motion results. Again, a larger temporal kernel size gives a larger bias and smaller reliability measure in the motion estimation. For increasing radius, $r\rightarrow\infty$, the motion asymptotically reaches a linear motion path. The corresponding bias also asymptotically reaches low values for $r\rightarrow\infty$.

Anisotropy correction. The influence of the point-spread function of a microscope is simulated in sequences with anisotropic Gaussian spots. The size in the axial direction differs from the size in the lateral direction ($\sigma^a/\sigma^l=3$) to simulate the difference in blurring by the microscope in the axial and lateral direction. Due to the blurring of the microscope, the intensity profiles of different spots can overlap. The derivative kernel widths are chosen as

$$\sigma_g^a/\sigma_g^l = 1/\sqrt{57}$$
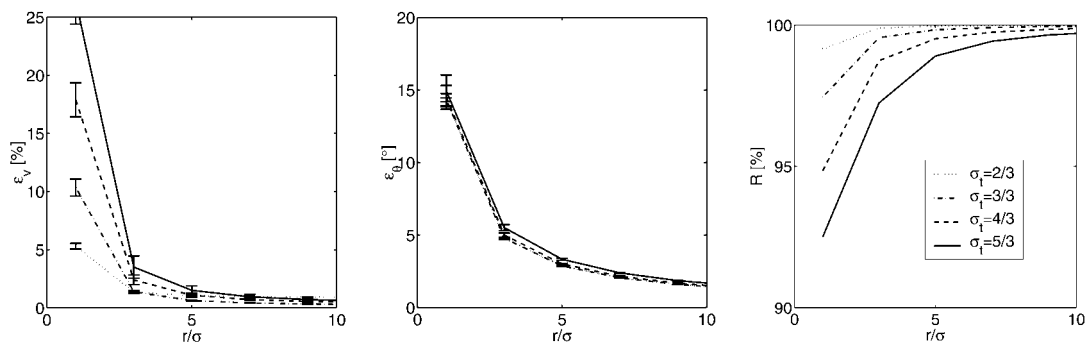
for a

$$\sigma_G/\sigma^l = 8/\sqrt{7}$$

to correct for the anisotropy of the spot. The spot describes a linear motion with constant velocity $|v| = 5.0\sigma^l$. A second spot is situated at a distance from the center of the moving spot at the time frame of estimation. Three situations are demonstrated: the second spot is located in the lateral plan ($\phi=0°$), the second spot is located in the axial plane ($\phi=90°$), and the second spot is located at $\phi=30°$ from the lateral plane (Fig. 6). This simulation is repeated with the same anisotropic spots but with isotropic derivative kernels.

Figure 7 shows the estimation bias for two overlapping Gaussian intensity profiles. The bias is calculated at the time frame where the distance d between the spots is minimal. The estimation bias is a function of d for both situations. The original anisotropic spot with isotropic derivative kernels also shows an orientation dependency (Figure 7, top). When the anisotropic spot is compensated with anisotropic kernels (Fig. 7, bottom), the orientation dependency vanishes. The reliability measure R drops below 90%, which is small compared with the other simulations described.

Robustness for intensity profile shape. Because the estimation method depends on the estimation of intensity derivatives, the shape of a spot is of interest. If the shape of a spot hampers accurate derivative estimation, the result of the estimation method may be biased. Spot

FIG. 5. Curved motion with constant velocity. For a moving Gaussian spot along a curved path with radius r, the velocity estimation errors ε_v and ε_θ and the reliability measure R are given as function of the radius r.
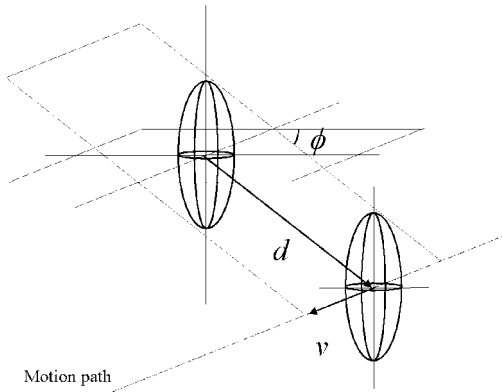
FIG. 6. The positioning of two spots for the simulation with two overlapping spots. One spot is fixed in space at the origin. The second spot moves along a straight line with a constant velocity v. The motion path has at a minimum distance d from the origin an angle Φ from the lateral plane.
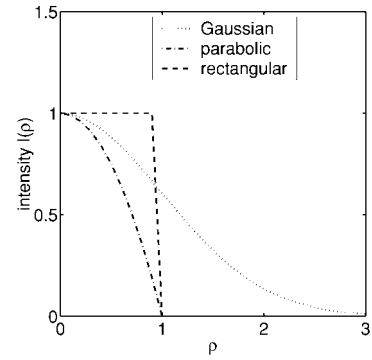

FIG. 8. Intensity profiles. A Gaussian-shaped intensity profile, a parabolic intensity profile, and a rectangular intensity profile. The profiles give the intensity of the objects as function of the radius from the center of the object.

shapes encountered in living cells will usually resemble a Gaussian spot shape. However, profile shapes that are more accurately described by a parabolic or even a rectangular intensity profile are sometimes present in the images. To examine the bias caused by spot shapes deviating from a Gaussian shape, three spot shapes are used: a

Gaussian-shaped spot as in the previous simulations, a spot with a parabolic intensity profile, and a spot with a rectangular intensity profile. Figure 8 shows the three intensity profiles that are used. The intensity is given as a function of the distance from the center of the object. Figure 9 shows the estimation bias for the three shapes. The bias for the three different shapes is negligible. The reliability measure is approximately 100%.
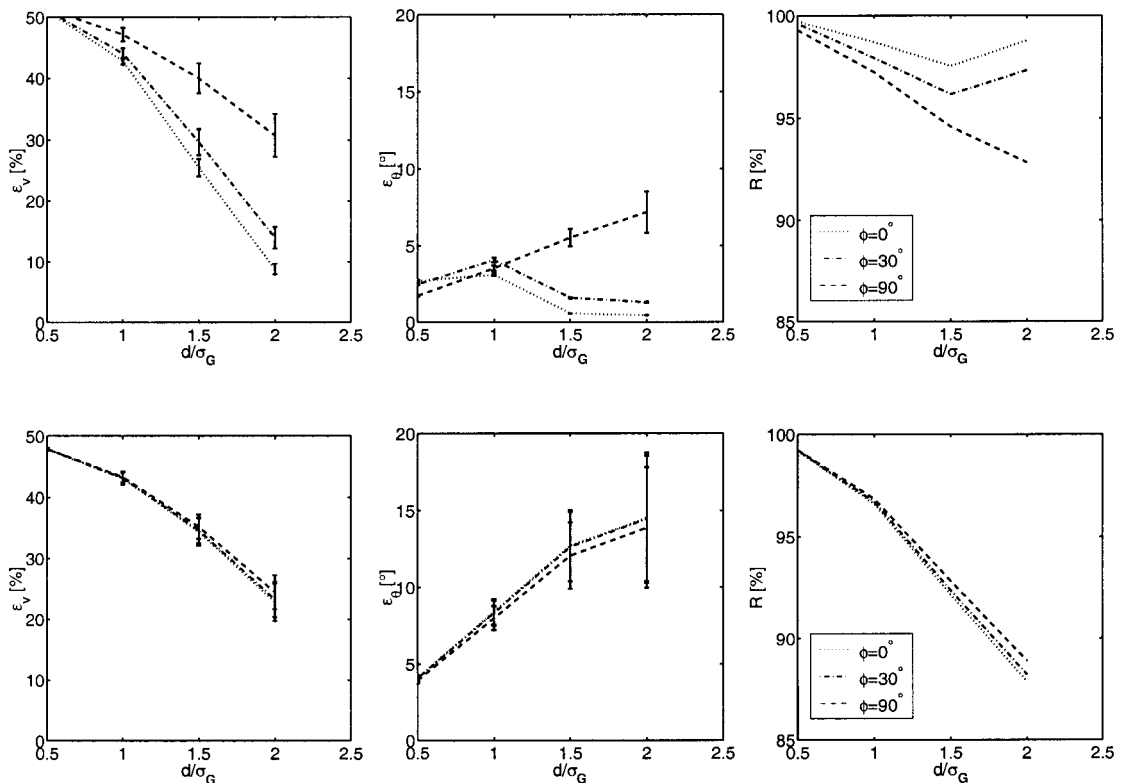

FIG. 7. Point-spread function influence: an anisotropic spot constantly moving along a straight line with another stationary spot overlapping. The location of the stationary spot at distance d/σ_G is taken for three angles φ with the lateral plane. **Top:** No correction for anisotropy is applied. **Bottom:** Correction for point-spread function influence.
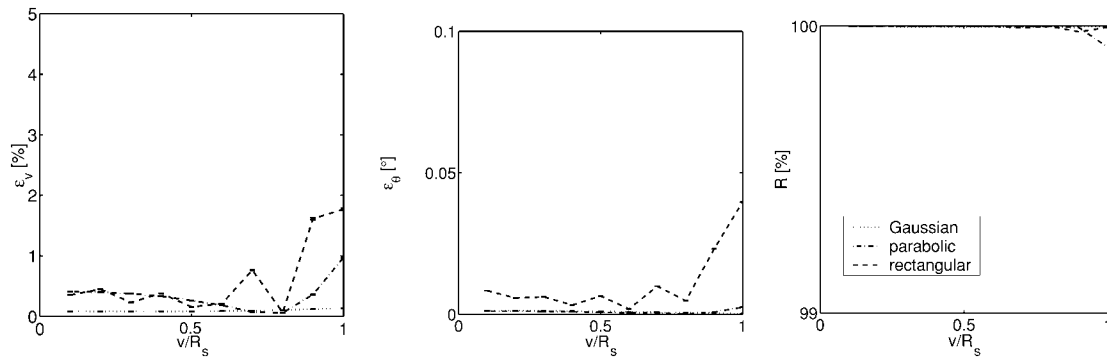
FIG. 9. Robustness for shape: the velocity errors ε_v and ε_θ and the reliability measure R are given for three different shapes, with radius R_s: an object with a Gaussian intensity profile, an object with a parabolic intensity profile, and an object with a rectangular intensity profile.

Application to 3D Confocal Image Sequences

Fluorescent bead. A series of linear motion paths is constructed from the series of bead images (Fig. 10), with velocities $|\mathbf{v}| \in [5,25]$ in the lateral plane. Figure 11 shows the resulting motion estimation bias along with the reliability measure R. The reliability measure R is never lower than 95%.

Living cell. The second sequence contains a living cell nucleus labeled with fluorescein-dUTP (Fig. 12). Spots formed from labeled DNA move through the nucleus. In the sequence, we observe that the cell shows a global motion containing translational and rotational components. Superimposed on this global motion, spots show a relative motion. Because we are only interested in the relative motion of the single spots, we corrected for nuclear movement.

Figure 13 (top right panel) shows five time steps of the sequence. The time steps are color coded. Each time step is obtained from the sequence by taking a threshold on the maximum intensity projection along the z-axis. This figure gives an impression of the motion paths. The motion paths of spots A and B show an approximately linear path for time steps 2, 3, and 4, whereas the motion path of spot C shows a meandering curve.

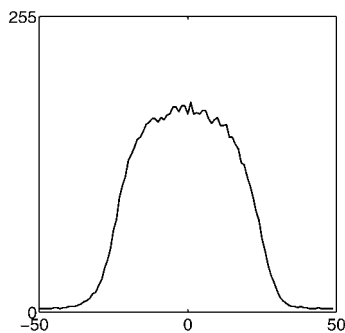The velocity of the spots is estimated using kernel sizes $\sigma_s=5$ and $\sigma_w=5$ for the spatial scale and $\sigma_t=2/3$ for the temporal scale. To represent the estimated velocities, the three spots A, B, and C in Figure 13 are shown in Figure 14. For each spot, two optical sections are presented: one optical section at a specific z position (x-y plane, left image) and one optical section at a specific x position (z-y plane, right image). In the optical sections, two time steps are shown as two colors. The first time step is colored red and the second time step is colored green. To give an idea of the estimated velocities, a smooth contour at a constant intensity (isophote) is plotted. The plotted velocity vectors for spots A and B start from the first contour and end near the second contour. The vectors show the direction and the length of the displacement of the spots. The velocity vectors are a projection of the 3D velocity vectors.

Spots A and B (Fig. 14, top and middle panels) show a good velocity estimation and spot C (Fig. 14, bottom panels) shows an inferior velocity estimation. Both direction and length of the velocity vectors of spot C do not correspond with the displacement of the spot due to the meandering of spot C. The values for the reliability measure for the three spots are measured. Spots A and B have a reliability of 99.6% and 94.0%, respectively. The reliability measure for spot C is 90.4%.

DISCUSSION

We demonstrated the usefulness of derivative-based velocity estimation in 3D confocal image sequences. Within the optical flow framework, we investigated the determinants for accuracy in velocity of spots in living cells. The characteristics of the motion patterns were of major importance for the correctness of the velocity estimation. We have extensively investigated the influence of the motion patterns on the bias of the velocity estimation method in a number of simulations.

The simulations confirm the theoretically derived unbiasness of the velocity estimation for constant linear motion. Therefore, constant linear motion is a good starting point for the analysis of other more complex motion patterns. Accelerated motion of spots introduces a bias in the estimated velocities, which increases with increasing acceleration and temporal support. Acceleration in the
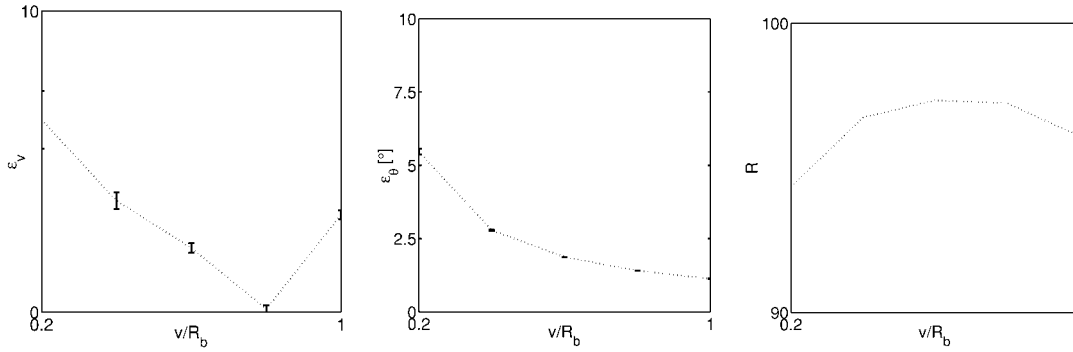

FIG. 10. The intensity profile along a line in the xy plane through the center of the recorded bead.

FIG. 11. Motion estimation on a single moving fluorescent bead. A bead with radius R_b of approximately 25 [voxel] is artificially moved with a constant velocity $|v|/R_b$ along a linear trajectory. The velocity estimation errors ε_v and ε_θ and the reliability measure R are given as function of the bead velocity $|v|/R_b$.

direction of motion introduces a bias due to the shape of the temporal intensity profile. The temporal intensity profile of an accelerated Gaussian spot is asymmetric whereas the temporal derivatives are symmetric functions. This asymmetry of the temporal intensity profile causes a bias in the velocity estimation. For motion with a constant tangential acceleration, the motion pattern describes a curve with a specific radius. A curved motion path also deviates from a linear motion path, introducing a bias on the velocity estimation. For small values of the radius of the curve and a large width of the temporal support, the bias increases significantly compared with linear motion.
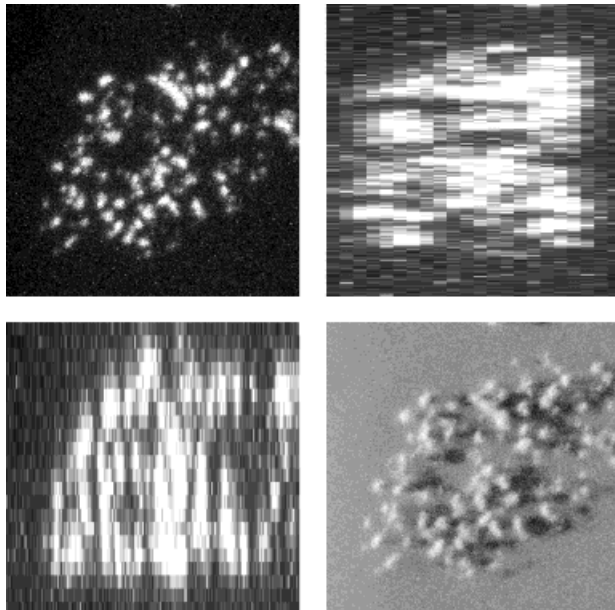

FIG. 12. A single frame from the live cell sequence. At the top left, top right, and bottom left, maximum intensity projections are shown of the recorded volume. The top left image is the xy plane, with the projection along the z-axis. The top right image shows the maximum intensity projection along the x axis. The bottom left image shows the projection along the y axis. The bottom right image shows a 3D impression by means of a simulated fluorescence process (SFP; 20).

The velocity estimation method assumes a constant shape of a single spot within the temporal kernel support. When the intensity profile of the spot is severely disturbed by a neighboring spot, large bias occurs in the velocity estimation. Consequently, situations should be avoided where spot intensity profiles change rapidly compared with the temporal sampling rate.

Apart from the motion pattern of spots, the point-spread function introduces a position and orientation dependency of the velocity estimation. For two overlapping spots, the influence of the point-spread function was compensated for by introducing anisotrope derivative kernels. In this way, the effective spot profiles become isotrope. By compensation, the spots assume a larger diameter, resulting in a larger bias. However, the resulting bias is predictable because the bias is independent of the relative position of two spots. Specifically combined with a possible correction method for the bias, this bias becomes independent of the relative orientation.

To investigate the dependency of the velocity estimation method on the shape of the intensity profile, we applied a rectangular, a parabolic, and a Gaussian intensity profile. Even in these cases, the bias for constant linear spot motion is negligible. Therefore, we conclude that the velocity estimation is not significantly dependent on the shape of the intensity profile of the spots as long as the shape is constant in time.

On a real image sequence, the motion estimation shows good velocity estimation for spots with a linear motion path as can be expected from theory and simulations. The experiment shows a close correspondence with simulations on linear motion. The bias observed for the fluorescent bead can be attributed to positional and intensity noise. For example, spots A and B in the image sequence (Fig. 13) of the living cell show an almost linear motion path within the kernel support of the temporal derivative, whereas spot C shows a meandering motion path. Consequently, the velocity estimation for spot C shows large errors compared with the velocity estimations for spots A and B. The motion of spot C is highly curved compared with the size of spot C. The order of magnitude in the bias
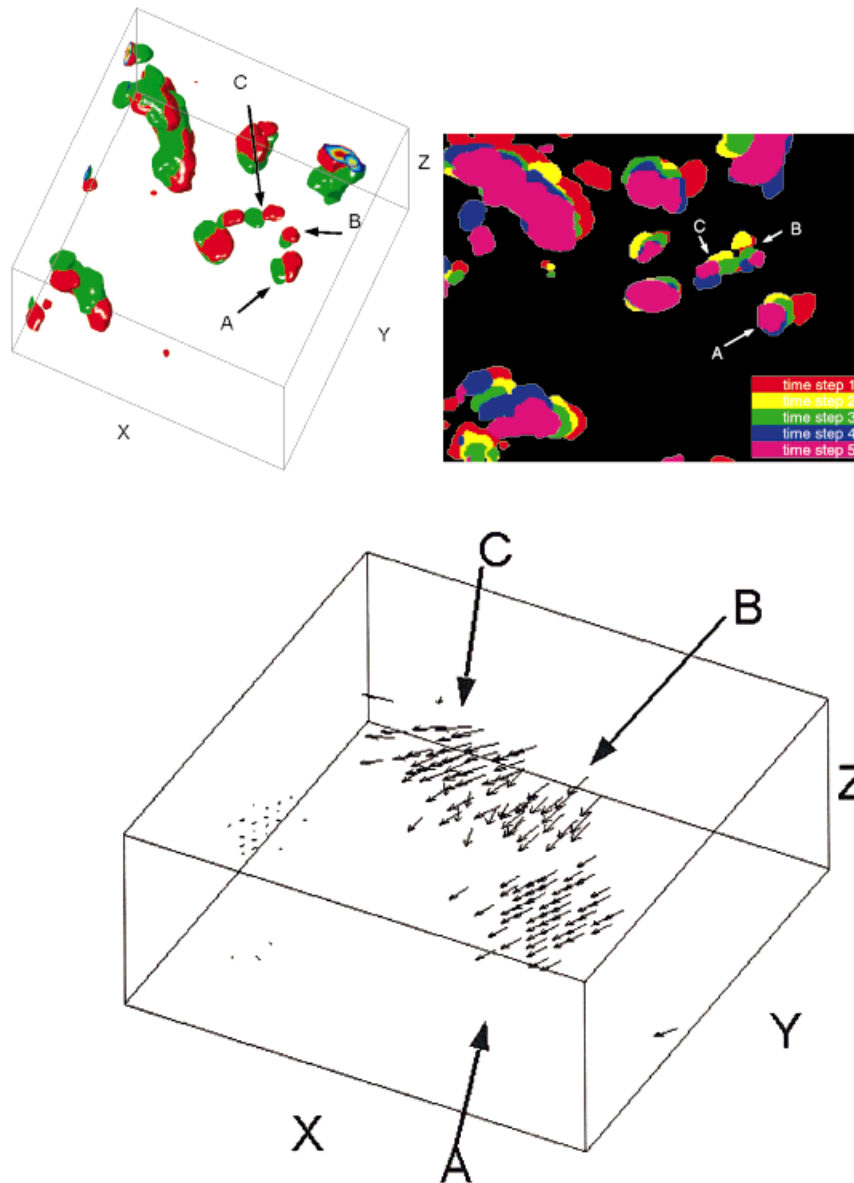
FIG. 13. **Left:** Two time steps coded red and green, respectively, in a 3D representation of the living cell. Red, first time step; green, second time step. **Right:** A maximum intensity projection of the 3D region. The projection shows a region of the cell at five time steps. Each time step is obtained as a maximum intensity image along the z axis. From this region, the velocity vectors are estimated. **Bottom:** A 3D representation of a part of the estimated velocity field around spots A, B, and C.

in both direction and length of the estimated velocity vectors is similar to the bias as found in the simulations (compare Figs. 5 and 14, bottom panels). The poor velocity estimation is also reflected in the value of R. In the application, R is low for spot C compared with the values of R for spots A and B.

The combination of the temporal kernel size and the temporal sampling is crucial for velocity estimation. For example, the combination in the application is clearly insufficient for spot C, whereas the combination is sufficient for spots A and B. Theoretically, for nonlinear motion such as for spot C, a small temporal kernel is favor-

able because the influence of changes in the velocity is small for a smaller temporal kernel size. However, a practical lower limit of the temporal kernel size exists due to the discrete nature of time sampling. This limit can be reduced by taking a high as possible temporal sampling rate. The change in velocity is then small for successive frames, resulting in a more linear motion path compared with the temporal kernel size.

With the velocity estimation method, a tool for estimating 3D velocity fields is presented which is successfully applied to a living cell spot sequence. With the estimated velocity fields, motion patterns can be observed.
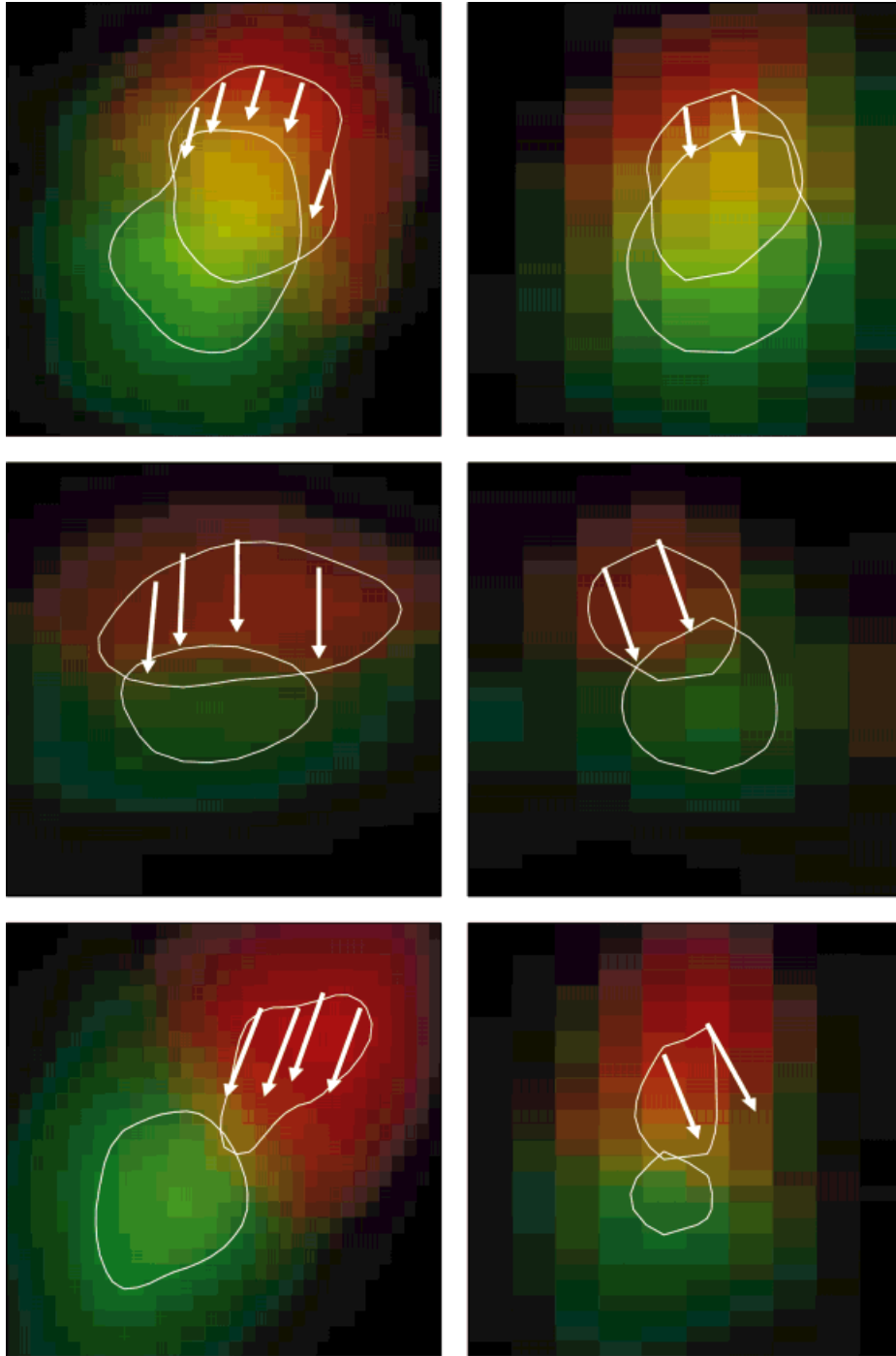
FIG. 14. Spots A, B, and C at two time steps from top to bottom, respectively. Estimated velocity vectors for the spots are projected in the x-y and z-y planes. **Left:** Images show an x-y optical section through the spot with the horizontal axis the x axis and the vertical axis the y axis. **Right:** Images show a z-y optical section through the spot with the horizontal axis the z axis and the vertical axis the y axis. The two time steps are color coded. The first time step is colored red and the second time step is colored green. For guidance, smooth isophote contours are plotted. The velocity vectors originating from isophotes are projected on the optical sections.

The bias is dependent on the size of the used kernels. In the simulations of nonlinear motion, the bias increases with increasing temporal kernel size. An extension of the work presented could be modeling the existing relation between temporal kernel size and bias for several types of motion (18,19). Whereas the bias in the work of Deriche and Giraudon (18) and Streekstra et al. (19) is on the position of corners and line structures, the modeling of the bias is analogous in the temporal direction. Modeling the bias as a function of the temporal kernel size enables one to correct

for the bias, because the amount of bias that is introduced by the temporal kernel size used can be estimated.

The dependency of the bias on the kernel size is disturbed when spots overlap because the bias also becomes direction dependent. Correcting for this anisotropy eliminates the direction dependency. This gives the possibility for correcting for the bias, without the influence of the direction of two overlapping spots.

The motion patterns in the velocity field are a starting point for analysis of living cell dynamics during cell division. From the velocity field, motion of the total nucleus is apparent. This nucleus motion is caused by cell migration during image acquisition. Furthermore, if several spots form a group with a common motion pattern, this is seen in the velocity field. The relative motion of a single spot compared with surrounding spots is also clear from the velocity field. Guided by the estimated velocity field, spots can be followed in time, creating spot trajectories in a 3D volume. These spot motion patterns and spot trajectories can play a role in the analysis of living cell dynamics (Manders et al., unpublished data).

ACKNOWLEDGMENTS

LITERATURE CITED

1. Sethi I K, Jain R. Finding trajectories of feature points in a monocular image sequence. IEEE Trans Pattern Analysis Machine Intelligence 1987;9:56–73.
2. Zheng Q, Chellappa R. Automatic feature point extraction and tracking in image sequences for arbitrary camera motion. Int J Comput Vision 1995;15:31–76.
3. Adelson EH, Bergen JR. The extraction of spatiotemporal energy in human and machine vision. Proceedings of IEEE workshop on visual motion. 1986. p151–156.
4. Barron JL, Fleet DJ, Beauchemin SS. Performance of optical flow techniques. Int J Comput Vision 1994;12:43–77.
5. Battiti R, Maldi EA, Koch C. Computing optical flow across multiple scales: an adaptive coarse-to-fine strategy. Int J Comput Vision 1991; 6:133–145.
6. Horn BKP, Schunk BG. Determining optical flow. Artif Intelligence 1981;17:185–204.
7. Lucas BD, Kanade T. An iterative image registration technique with an application to stereo vision. Proceedings of imaging understanding workshop. 1981. p121–130.
8. Simoncelli EP, Adelson EH, Heeger DJ. Probability distribution of optical flow. Proceedings of the conference on computer vision and pattern recognition. 1991. p 310–315.
9. Strasters KC. Quantitative analysis in confocal image cytometry. PhD thesis, Delft University of Technology, 1994.
10. van Kempen GMP. Image restoration in fluorescence microscopy. PhD thesis, Delft University of Technology, 2000.
11. Manders EMM, Kimura H, Cook PR. Direct imaging of DNA in living cells reveals the dynamics of chromosome formation. J Cell Biol 1999;144:813–821.
12. Weber J, Malik J. Robust computation of optical flow in a multi-scale differential framework. Int J Comput Vision 1995;14:67–81.
13. Niessen W. Multiscale medical image analysis. PhD thesis, University Utrecht, 1997.
14. Lindeberg T. Scale-space theory in computer vision. Kluwer; 1994.
15. Bergsma CBJ, Streekstra GJ, Smeulders AWM. Single spot motion estimation. ISIS technical report, University of Amsterdam, 2000.
16. Joliffe IT. Principal component analysis. New York: Springer-Verlag; 1986.
17. van Vliet LJ. Grey-scale measurements in multi-dimensional digitized images. PhD thesis, Delft University of Technology, 1993.
18. Deriche R, Giraudon G. A computational approach for corner and vertex detection. Int J Comput Vision 1993;10:101–124.
19. Streekstra GJ, van den Boomgaard R, Smeulders AWM. Scale dependent differential geometry for the measurement of center line and diameter in 3D curvilinear structures. Proceedings of the international conference on scale-space theories in computer vision. Lecture Notes Computer Sci 1999;1682:500–506.
20. van der Voort HTM, Noordmans HJ, Messerli JM, Smeulders AWM. Physically realistic volume visualization for interactive analysis. Proceedings eurographics. 1993. p 295–306.